Engineering Fracture Mechanics 326 (2025) 111393

Contents lists available at ScienceDirect

Engineering Fracture Mechanics

journal homepage: www.elsevier.com/locate/engfracmech

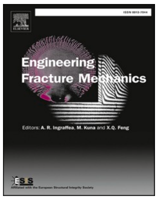

Hygrothermal degradation of modes I and II fracture toughness in flat carbon/epoxy composites: experimental and numerical insights

Leonardo G. Schreer [a,b], Antonios G. Stamopoulos [c], Paweł Stabla [d], Michał Smolnicki [d], Sandro C. Amico [b], José Humberto S. Almeida Jr [e,*]

[a] *SENAI Institute of Innovation in Polymer Engineering, São Leopoldo, Brazil*
[b] *PPGE3M/Federal University of Rio Grande do Sul, Porto Alegre, Brazil*
[c] *Department of Industrial and Information Engineering and Economy, University of L'Aquila, Montelucco di Roio, Italy*
[d] *Faculty of Mechanical Engineering, Wroclaw University of Science and Technology, Wroclaw, Poland*
[e] *Department of Mechanical Engineering, LUT University, Lappeenranta, Finland*

ARTICLE INFO

Keywords:
Hygrothermal ageing
Fracture toughness
Material characterisation
Filament winding

ABSTRACT

Filament winding is a widely used technique for manufacturing axisymmetric fibre-reinforced composites, such as pressure vessels and pipes, designed for harsh environments. Understanding the effects of these conditions on mechanical performance is crucial. This study presents a combined experimental and numerical investigation of unidirectional carbon/epoxy composites manufactured via filament winding, subjected to tensile, compressive, shear, and interlaminar fracture toughness tests (Modes I and II). Samples were exposed to hygrothermal ageing at room and elevated temperatures to assess moisture absorption and its influence on fracture properties. Special attention is given to the variation in interlaminar fracture toughness as a result of hygrothermal exposure. A fractographic analysis reveals fibre bridging as a key mechanism behind enhanced Mode I toughness, while Mode II toughness deteriorates with ageing. The findings provide critical insights into the durability and failure mechanisms of filament-wound composites under service conditions.

1. Introduction

The continuously growing demand for materials with superior properties that can perform under demanding ecological and economic conditions is evident. In this context, composite materials have been implemented in increasing applications due to some unique features they provide to the industry, including a high strength-to-weight ratio, increased stiffness, increased fatigue life and design flexibility [1]. Another interesting fact is the presence of a variety of manufacturing methods for producing composite components. Among these methods, the filament winding process is an appealing solution for producing axially symmetrical structures, including tubes, pipelines and even pressure vessels [2–4]. This process involves depositing pre-impregnated fibre-reinforced polymeric tapes into a rotating mandrel at determined speeds for creating repeated patterns [4–6]. Despite the flexibility and versatility of this manufacturing method, the composites are prone to several defects such as gaps between the deposited tows [2], porosity [7], fibre

---

[*] Corresponding author at: Department of Mechanical Engineering, LUT University, Lappeenranta, Finland.
E-mail address: Humberto.almeida@lut.fi (J.H.S. Almeida Jr).

https://doi.org/10.1016/j.engfracmech.2025.111393
Received 26 March 2025; Received in revised form 18 June 2025; Accepted 7 July 2025

Nomenclature

E_{1f}	Longitudinal flexural modulus
G_{IC}	Mode I critical energy release rate
G_{IIC}	Mode II critical energy release rate
G_Q	Total energy release rate at a given loading condition
P_{Max}	Maximum load during the crack progression
a_0	Crack length at the time of fracture
t_0	Initial time
CC	Compliance Calibration
FW	Filament winding
h	Half of the thickness
C	Compliance
F	Correction factor
P	Load
$U(max)$	Maximum moisture absorption
$U(t)$	Moisture absorption
a	Crack length
b	Width
k	Growth rate
m	Compliance calibration coefficient
t	Time
δ	Longitudinal displacement

angle deviation [4,8], while the overall mechanical behaviour is dependent on several factors including the generated pattern [8,9] or the stacking sequence/winding type that modifies the filament tension during the deposition [10,11] and the overall compaction of the layers [12].

Since a potential component made of these material systems should perform well under various environmental conditions, their mechanical performance after being exposed to hostile environments is of paramount importance. It can be noticed that an increasing number of studies have identified the effects of temperature and humidity on the material structure and mechanical behaviour. As stated by Dao et al [13], moisture absorption may activate irreversible chemical changes in the composite structure due to the reaction of the polymeric system and the water, influencing the ageing process as well. These reactions may be in the fibre–matrix interface, affecting the load transfer from the matrix to the adjacent fibre bundles [14]. As reported by Garg and Chalak [15], several factors affect the humidity uptake, such as exposure resistance, relative humidity, temperature, component geometry, loading conditions or even the fibre content. In detail, the absorption is found to be increased in lower fibre volume fractions. As seen in past works [16], the moisture absorption is closely dependent on manufacturing defects such as porosity, which is already known for degrading the matrix-dominated properties [17,18]. Therefore, the spherical assessment of the effects of exposure to a potential thermal variation, as well as to a humid environment, under various loading conditions is crucial.

In the same context, the interlaminar fracture toughness of composite materials, when exposed to hygrothermal conditions, is of interest. Davidson et al. [19] studied double cantilever beam (DCB) samples of carbon/epoxy composites under a combination of saturated humidity and temperatures from −43 to 125 °C. The results indicated an increase in the critical energy release rate G_{IC} while the temperature increased, and a change in the morphology of the R-curves while the G_{IIC} values decreased. The same statement about the moisture effects was previously observed in the works of Sezler and Friedrich [20], Garg and Ishai [21] and Fishcer and Arendts [22], which is attributed to a combination of phenomena including matrix plasticisation, fibre bridging and intense coalescence of microcracks near the crack tip. The enhancement of the matrix ductility is also stated by Khan et al. [23], however, without an increase in the G_{IC} values.

In the case of cylindrical filament-wound structures, curved samples have traditionally been used for measuring interlaminar fracture toughness. However, only a limited number of studies have employed such configurations due to the complexity of specimen geometry and the challenges associated with manufacturing and testing [24–28]. For example, Pollet et al. [29] investigated the effect of hygrothermal ageing on Mode I fracture using curved double cantilever beam (CDCB) specimens, revealing significant R-curve changes due to humidity and temperature exposure. As an alternative, filament-wound flat specimens offer easier characterisation setups but pose considerable manufacturing challenges, particularly regarding tow placement and compaction. Previous studies have focused on tensile behaviour [30] or fatigue performance [31] of such flat configurations, with minimal attention to fracture toughness. Moreover, Ribeiro et al. [32] applied numerical models to curved wound structures but did not extend this to hygrothermal degradation or flat specimens.

This study provides a comprehensive and systematic evaluation of Mode I and Mode II fracture toughness of flat carbon/epoxy composites after hygrothermal ageing, combining experimental mechanics, fracture surface analysis, and finite element simulations calibrated with experimental data. This is one of the first studies to assess the interplay between moisture absorption, thermal ageing, and crack propagation in flat laminates manufactured by filament winding. The use of experimentally calibrated R-curve-based numerical models enhances novelty, being a practical and effective predictive tool for interlaminar failure under service conditions relevant to composite pressure vessels.

2. Materials and manufacturing

2.1. Materials

The materials used for the manufacturing of the composites were continuous unidirectional carbon fibre towpregs pre-impregnated with a thermosetting epoxy resin from the manufacturer SGL Carbon. The towpregs, with the code CT24-5.0/270-E100, were produced by SIGRAFIL, and the epoxy matrix, with the code E910, was supplied by SIGRAPREG. The fibre filaments are untwisted and have an average width of 6.4 mm, containing 24 K filaments with an average diameter of 6.9 μm. The pre-impregnated tow contains a fibre volume fraction of 65%.

2.2. Manufacturing of standard laminates

The unidirectional laminates were manufactured using a seven-axis robotic fibre placement system (model Kuka KR 140 L100-2) to ensure precise control of fibre alignment, tension, and deposition quality. Its control capabilities enable precision and quality in the placement of the towpregs, achieving a winding angle tolerance of 0.5%, corresponding to a minimum positioning accuracy of 0.1 mm. Although flat specimens were used in this study, the robotic process is typically applied to complex geometries such as tubes, cylinders, and composite overwrapped pressure vessels (COPVs). Employing the same manufacturing route for flat panels ensures that the measured mechanical properties are representative of those achievable in curved structural components, enhancing the relevance and transferability of the results to real-world applications.

The laminate designs were created using the CADWind 2010 software, which is dedicated to the design and manufacturing of filament-wound components. The software functions range from CAD model creation, where the component is designed, to post-processing the model to generate codes applicable to winding the part.

A rectangular stainless-steel plate was designed and produced ($327 \times 228 \times 12$ mm^3) to serve as the mould, enabling the production of unidirectional carbon/epoxy laminates. To facilitate the removal of the laminate after material curing, a Loctite Frekote 770-NC release agent was applied to the mandrel. To meet the laminate thickness requirements of the adopted standards, laminates with 3 and 4 layers were manufactured. After the winding process was completed, the mandrel/laminate assembly was wrapped with shrink tape to promote laminate compaction. Consecutively, to obtain a laminate with similar quality to cylindrical laminates, the laminates were pressed in a heated hydraulic press under a pressure of 6 ton and heated at 4 °C/min to 140 °C and held for 45 min. The curing process was carried out under constant pressure, with the heated press, mandrel, and laminate subsequently cooling down to room temperature at a rate of 4 °C/min.

2.3. Manufacturing of laminates for fracture tests

The manufacturing procedure for the test specimens for interlaminar fracture toughness in Modes I and II was like those previously described in Section 2.2. However, 16 layers of material were used to reach the thickness recommended by the ASTM D5528 and the ASTM D7905 standards (3.5 to 5 mm). The process can be divided into three stages: the first involves winding 8 layers. The next stage was applying a 0.13 mm-thick PTFE release film (from Armalon) at the mid-plane of the laminate to induce a pre-crack, as seen in Fig. 1 (a), with a width of 65 mm, specifically for Mode-I testing, ensuring that the distance between the load application centre and the end of the film is 50 mm. Finally, another 8 layers are wound (Fig. 1(b)), achieving the production of a 16-layer lamina, reaching an approximate thickness of 4 mm.

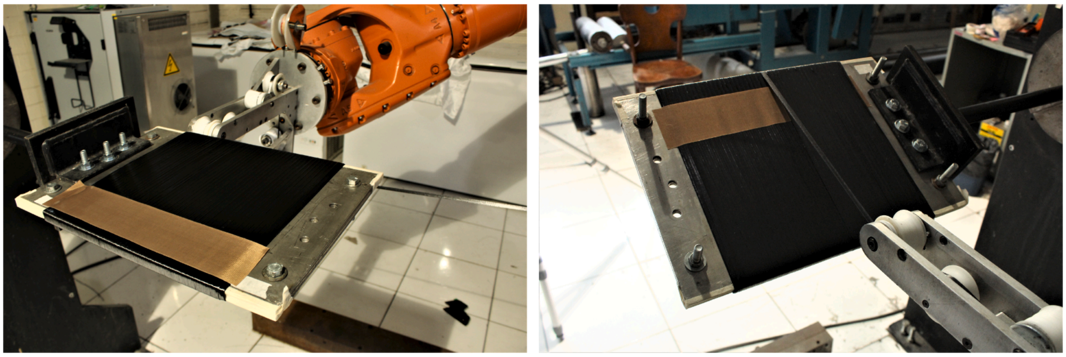

(a) (b)

Fig. 1. (a) Winding of laminates for fracture tests paused after deposition of layer 8 to insert the releasing film, and (b) continuation of depositing the remaining 8 layers.

3. Testing

3.1. Hygrothermal conditioning

To analyse the effects of hygrothermal conditioning on fracture toughness results, five samples per group were produced as previously described and, subsequently, submerged in water at either room temperature (23 °C) or 70 °C. The choice of the temperatures of interest was based on previous works in the field [28,32]. Before hygrothermal conditioning, the samples were dried in an oven at 90 °C for 24 h to remove any initial moisture. These dried samples serve as the reference condition throughout the study, providing a baseline for comparison with the aged specimens. After drying, the samples were weighed and placed back in the oven for an additional hour, followed by another weighing. This step was repeated until the total mass stabilised, averaging 4 h, with the final weight being recorded as the dry sample weight.

Moisture absorption was monitored according to the guidelines of the ASTM D5229 standard, with regular weighings until all sample groups reached mass stabilisation. Consequently, during the first few days of conditioning, when absorption was faster, the measurement frequency was twice a day, while after several days, the frequency was reduced to once a day and, eventually, to every three days. Overall, roughly 900 h were required to reach a total stabilisation and the “effective equilibrium”, that is, a mass variation of less than 0.02% between two consecutive measurements. The calculation of mass variation is represented by:

$$\Delta M(\%) = \left(\frac{M_{final} - M_{initial}}{M_{initial}}\right) \times 100 \tag{1}$$

Mass stabilisation can also be observed and determined graphically from the plateau zone of the moisture gain (as a percentage of mass) against the square root of time.

In order to fit the experimental data points, three models are employed based on their ability to represent non-linear, saturation, or growth behaviour:

1. Sigmoidal model (logistic function)

$$U(t) = U_{\max} \cdot \frac{1}{1 + e^{-k(t-t_0)}} \tag{2}$$

where $U_{\max}$ is the maximum moisture absorption, k is the growth rate, t is time and t_0 is the inflection point.

2. Polynomial model (third-order polynomial)

$$U(t) = a + b \cdot t + c \cdot t^2 + d \cdot t^3 \tag{3}$$

Where coefficients a, b, c, d are determined by fitting to the data.

3. Exponential saturation

$$U(t) = U_{\max} \cdot \left(1 - e^{-k \cdot t^n}\right) \tag{4}$$

where n is the scaling exponent.

A statistical assessment of the suitability of the fitted data is performed and determined in terms of root mean square error (RMSE) and the coefficient of determination (R^2).

3.2. Material characterisation tests

Test specimens were subsequently machined following the specifications of the ASTM D3039 for tensile tests of unidirectional composites oriented at 0° or 90° ($250 \times 15 \times 1.5$ mm^3 and $175 \times 25 \times 1.5$ mm^3, respectively), the ASTM D6641 for compression tests of unidirectional composites oriented at 0° or 90° ($140 \times 12.7 \times 2.3$ mm^3 for both), and the ASTM D7078 for in-plane shear tests with double-notched specimens ($76 \times 56 \times 4$ mm^3) [33]. For the tensile and compression samples, glass fibre-reinforced epoxy tabs were adhesively bonded to their ends, as recommended by the respective standards, using the 3M™ Scotch-Weld™ epoxy adhesive DP460N. All the specimens were CNC-machined after the tabs were applied to ensure proper alignment.

The mechanical characterisation of the flat composites was carried out using an Instron Universal Electromechanical machine, model 3382, with a 100 kN load cell. The test speeds used were those recommended by the respective standards for each test, except for the compression tests, which were conducted at 0.8 mm/min for the 0° samples and 1 mm/min for the 90° samples to meet the requirements of the corresponding standard related to the test duration. Mechanical extensometers were used to obtain longitudinal and transverse strains in tension to calculate elastic constants. For the V-Notched test, a strain gauge rosette, model KFG-5–120-D17-11 from KYOWA, aligned at ±45°, was placed on the midsection of the sample.

3.3. Fracture toughness tests

The cutting procedure for these samples was carried out using the same CNC machine previously mentioned, with samples having dimensions of 25 × 150 × 4 mm^3 for Mode-I interlaminar fracture toughness and 20 × 180 × 4 mm^3 for Mode-II samples, as specified by the corresponding standards, which are ASTM D5528 and ASTM D7905 for modes I and II, respectively.

3.3.1. Mode-I fracture tests

The Mode-I interlaminar fracture toughness test is based on the application of a longitudinal load normal to the crack plane, promoting a purely Mode-I fracture in the semi-beam. The crack length, a, is monitored and correlated with the load (P) and longitudinal displacement (δ) during the test duration. For the proper load application, the loading block concept was used, using small aluminium blocks with dimensions of 30 × 30 × 25 mm^3 and a central hole of 13 mm diameter on the square face. For bonding the blocks to the specimens, the same DP460N structural adhesive from 3M™ was used, applying a thin film with a brush to ensure uniform distribution and thickness. In addition, the side of the samples was painted white to enhance the accurate visual observation of the crack tip. After painting, markings were placed every 1 mm for the first 5 mm (after the end of the PTFE film) and every 5 mm for the rest of the sample,

The tests were conducted on the same Instron Universal Electromechanical machine at a speed of 1.5 mm/min. The crack progression was monitored using a travelling digital microscope. The Modified Beam Theory (MBT) was adopted for the calculations [39], as follows

$$G_{Ic} = \frac{3P\delta}{2b(a+|\Delta|)} \tag{5}$$

where b is the width of the specimen, while a is the crack length. Since it is necessary to account for the rotation of the sample during the procedure, the crack length is corrected by the rotation correction factor Δ that can be obtained by plotting the compliance $C = \delta/P$, and the crack length. Thus, Δ is determined by the intersection of the regression line of the graph with the horizontal axis.

Another correction suggested by the ASTM D5528 standard, when using metal blocks to apply the load, is defined by the parameter F. This parameter accounts for the longitudinal distance from the load application point to the midpoint of the semi-beam thickness, expressed by:

$$F = 1 - \frac{3}{10}\left(\frac{\delta}{a}\right)^2 - \frac{3}{2}\left(\frac{\delta t}{a^2}\right) \tag{6}$$

where t is the distance between the centre of the loading block and the thickness neutral plane of the sample. The parameter F is then multiplied by the value of G_{Ic}, generating a new energy value with all corrections applied. For the determination of the critical energy release rate, the VIS point technique is applied, which is justified by the presence of a comparably less ductile matrix system of the composite material of interest, as seen in [34] as well.

3.3.2. Mode-II fracture tests

The Mode II interlaminar fracture toughness test uses a 3-point bending fixture with a span of 100 mm, where the specimen containing the release film is loaded to induce a purely Mode II fracture in the mid-plane of the laminate. The standard provides three different methods for determining fracture energies, two of which were used in this study. The first method is known as non-pre-cracked toughness (NPC), where the test does not feature an actual crack, but rather a crack-inducing insert. The second method is pre-cracked toughness (PC), in which the test is performed on a specimen that has already experienced a fracture. Typically, PC tests are conducted on samples that have already undergone NPC testing.

As with the previous tests, white paint was applied to each side of the specimen using a white automotive spray to introduce a thinner layer of paint to make the crack progression visible. The standard recommends making four different marks: one indicating the end of the PTFE film and the other three at distances that serve as reference points for the load cycles necessary to perform the test according to the CC method outlined in the standard. The equation used to calculate energy based on the CC method is expressed as:

$$G_Q = \frac{3mP_{max}^2 a_0^2}{2B} \tag{7}$$

where P_{max} is the maximum load supported by the specimen at the moment of crack progression, a_0 is the crack length at the time of fracture (typically 30 mm), B is the width of the specimen, and m is the coefficient obtained from compliance calibration. The subscript Q in G_Q indicates that certain loading conditions must be met for the energy values to be representative, meaning that $G_Q = G_{IIc}$, as described next.

The CC method uses experimental compliance data from the specimen at different crack lengths (a_j) through the linear regression of the curve plotting compliance against the cube of crack length ($C \times a^3$). To obtain a trend line, at least three different compliance coefficients of the structure are required, obtained from the crack lengths defined by the markings. Consequently, the flexibility parameters were obtained through three static flexural test cycles at a speed of 0.5 mm/min for crack lengths (a_j) of 20 mm and 40 mm, where the specimen was loaded up to a load P_j and then unloaded at the same speed. The loading cycle for the specimen with a crack length of 30 mm is called the “fracture test”, where the specimen is loaded until crack progression occurs. The maximum load in the first two cycles (P_j) can either be inferred analytically by

$$P_j = \frac{2B}{3a_j}\sqrt{G_{IIc}E_{1f}h^3} \tag{8}$$

where E_{1f} is the longitudinal flexural modulus and h is half the thickness of the laminate. If P_j is inferred experimentally, the maximum load P_{max} during the test must satisfy the G_q conditions introduced earlier, in which

$$\%G_Q = \left[\frac{100\left(P_j a_j\right)^2}{\left(P_{max} a_0\right)}\right]; j = 1 \tag{9}$$

where $15 \leq \%G_Q \leq 35$. Here, $j = 1$ corresponds to parameters with $a = 20\ mm$ and $j = 2$ with $a = 40\ mm$. If any value of $\%G_Q$ falls within the above parameters, it is possible, through a fracture test ($a_0 = 30$ mm), to determine $\mathrm{P_{max}}$ and isolate $\mathrm{P_j}$ for $j = 1, 2$. In this work, $\mathrm{P_j}$ was initially defined analytically using parameters obtained from material characterisation and literature data and was later adjusted with the results from the first sample of each family. With the loads $\mathrm{P_j}$ defined and the flexural tests conducted for the three crack lengths, the compliance against the cube of the crack length graph can then be plotted to obtain the trend line, defined as

$$C = A + ma^3 \tag{10}$$

where m and A are parameters used in Equation (11) to infer the crack propagation distance in the fracture tests to be used in the PC tests, which are discussed next.

The PC tests, if performed on the same samples as the NPC tests, require the compliance data from the specimen obtained in the last unloading cycle (C_u), immediately after crack progression. At this stage, the calculated crack length is estimated using Equation (11)

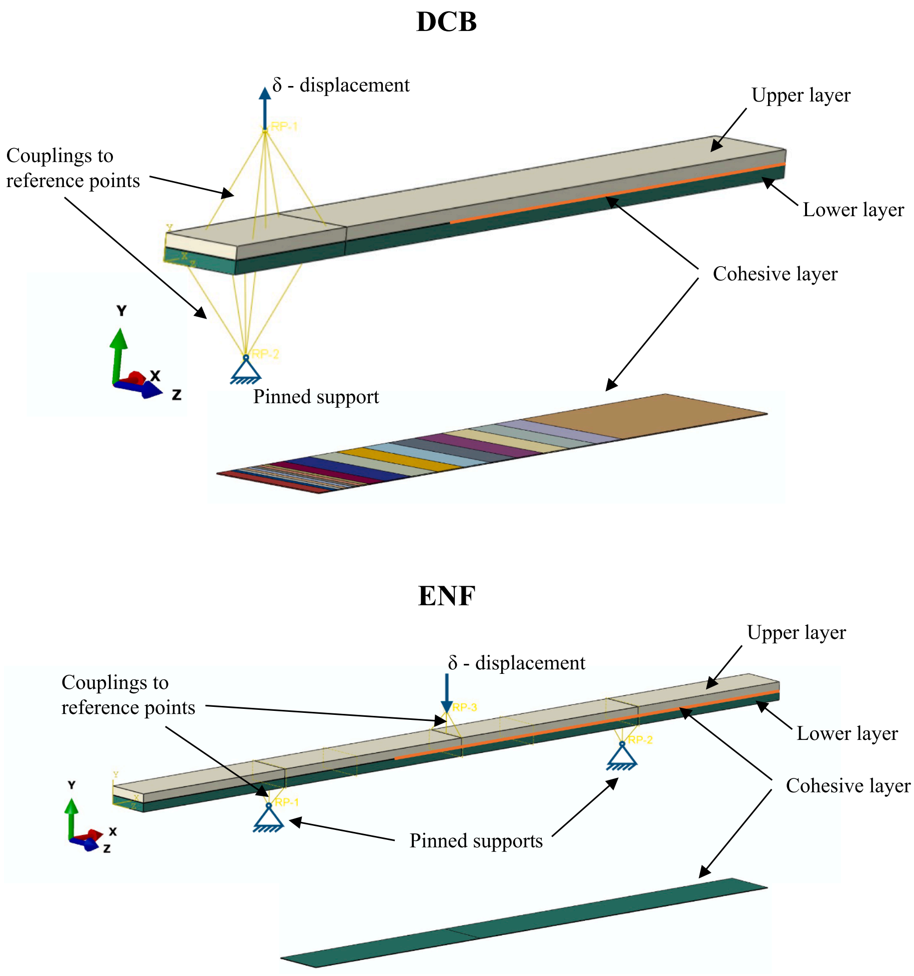

Fig. 2. The partitioned cohesive layer according to the variations in fracture energy release rate.

$$a_{calc} = \left(\frac{C_u - A}{m}\right)^{1/3} \tag{11}$$

This measurement is made from the crack tip to the marking of $a_0 = 30\ mm$. The remaining parameters A and m are obtained from the linear regression of the compliance graph, represented by Equation (11). In addition to analytically inferring the final crack length after progression, this parameter is also observed visually (a_{vis}) with the aid of a digital microscope. If the visual crack length a_{vis} is greater than a_{calc}, or if the crack tip passes the central loading point of the 3-point bending test, this length is used as the crack size, and new markings are made from this point to calibrate the compliance for the PC test. The entire process is then repeated to obtain the energies.

4. Finite element modelling

Finite element (FE) analysis was executed on the powerful Abaqus FE platform, unlocking unparalleled capabilities in defining fracture phenomena in composite materials. By leveraging a cohesive zone model (CZM), the fracture behaviour in both DCB and ENF experiments was captured with remarkable precision.

A robust 3D solid element model was employed, where composite layers were meshed with C3D8R elements and the cohesive regions with COH3D8 elements. To maximise simulation efficiency, the mesh was strategically refined in zones expecting crack propagation and coarsened elsewhere. Six finite elements through the composite thickness ensured depth accuracy, while a single cohesive element sufficed for the fracture zone.

An accurate representation of the mechanical behaviour hinged on meticulous material property assignment. Composite parameters were defined as engineering constants based on comprehensive experimental data carried out in this work. For the cohesive zones, the process began by setting the elastic properties in Abaqus under “Traction” by specifying longitudinal elastic modulus (E_1) and shear moduli (G_1 and G_2), with the transverse elastic modulus (E_2) selected to address tension perpendicular to the fibre direction. The next step integrated the bilinear traction-separation law parameters. The transverse tensile strength (X_{2T}) served as the maximum stress initiating delamination, while in-plane shear stresses (S_{12}) determined the nominal shear limits. The fracture energy then completed the traction-separation law framework. The numerical models for both the DCB and ENF tests are shown in Fig. 2. The boundary conditions (BCs) for the DCB model include two key components. First, a pinned support is applied to a reference point coupled with the lower layer of the specimen, representing the actual bonding surface between the composite and the glued aluminium block in the experimental setup. Second, a displacement-controlled reference point is coupled with the upper layer, simulating the movement of the second aluminium block. The numerical model takes advantage of the geometric symmetry of the test specimens; therefore, only half of the setup was modelled along the fibre-direction symmetry plane for both DCB and ENF simulations.

Capturing the R-curve effect, that is, the dynamic relationship between fracture energy and crack length, was critical, particularly in the DCB test. The cohesive zone model implemented in this study incorporates the R-curve effect by spatially varying the fracture energy, following the methodology developed in our previous work [35]. This approach enables the finite element model to more realistically represent the increase in fracture resistance during crack propagation, in contrast to conventional models assuming a constant fracture energy. To reflect this behaviour, the fracture process zone was partitioned into sub-sections, each assigned a specific fracture energy release rate (see Fig. 2 and Fig. 8). Hygrothermal ageing effects were incorporated by adjusting these locally defined energy release rates according to experimental measurements under different environmental conditions. Thus, the partitioned geometry not only captures the R-curve behaviour but also allows the integration of environmental degradation effects into the FE model.

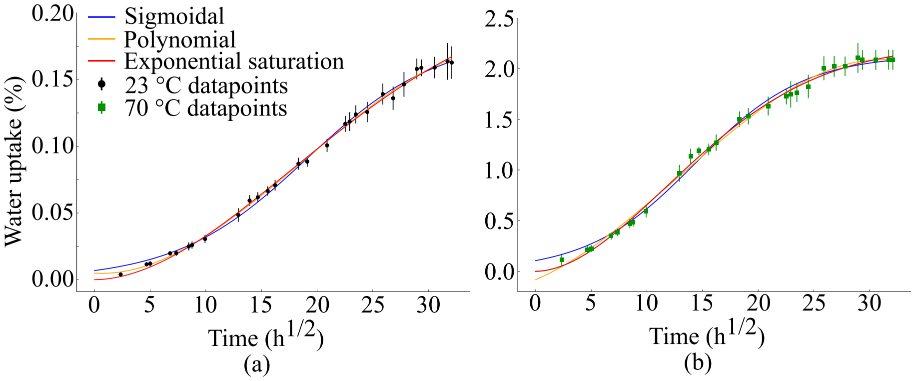

(a) (b)

Fig. 3. Moisture absorption for samples under (a) room and (b) hot temperatures: experimental datapoints and fitting models. Graphs with different Y-axis limits for better visualisation.

5. Results

5.1. Moisture absorption

Fig. 3(a-b) presents the experimental datapoints fitted with sigmoidal, polynomial and exponential saturation models. A significant difference in moisture absorption was observed for the samples aged at room temperature and 70 °C. At 23 °C, moisture absorption is slower and gradually reaches equilibrium. At 70 °C, faster diffusion is driven by increased molecular mobility, but lower equilibrium moisture results from reduced water-polymer interactions and solubility at higher temperatures. These effects highlight the complex interplay of thermal, chemical, and physical factors in the moisture absorption behaviour for these CFRP composites.

In addition to the experimental data, three models were used to fit them, and the initial guesses are presented below, while the optimum parameters are presented in Table:

- Sigmoidal model: U_{max}=2.0; k=0.1, t_0=10.
- Polynomial model: initial guesses derived from data trends.
- Exponential saturation model: U_{max}=2.0; k=0.01, n=1.

The optimum fitting parameters of every model are presented in Table 1, while Table 2 shows the statistical metrics of every model. Overall, at 23 °C, the exponential saturation model delivers a slightly superior fit compared to the other models. Its ability to capture gradual equilibrium behaviours aligns well with the data at this temperature. At 70 °C, the polynomial model emerges as the best performer, although the differences between models are minimal, highlighting the robustness of all approaches. Generally, the sigmoidal model is well-suited for datasets exhibiting inflection points and saturation behaviours. While slightly less flexible than other models, it consistently provides reliable fits across temperatures. The polynomial model stands out for its adaptability and precision, particularly at higher temperatures. However, it lacks the physical interpretability inherent to sigmoidal or exponential models. The exponential saturation model strikes a balance between accuracy and physical realism, making it ideal for scenarios where diffusion-like behaviours dominate.

In case one of the models needs to be selected by application, the exponential saturation model is used for applications requiring physics-based interpretation, such as diffusion and equilibrium modelling. On the other hand, the polynomial model is recommended when the goal is to capture trends with maximum flexibility, especially for higher-temperature conditions where trends approach linearity. Overall, in case a unified model needs to be suggested for such applications across temperatures, the sigmoidal model is a robust and versatile option, providing consistent performance while accommodating inflection and saturation behaviours.

5.2. Elastic and strength properties

Regarding the static tests, for tensile loading at 90°, the samples predominantly exhibited lateral failure, while longitudinal (0°) samples displayed a more explosive fracture, characterised by cracks dispersed across various regions of the specimen. Both failure patterns align with the acceptable criteria outlined in ASTM D3039. In the case of compression loading (CLC tests), failure occurred following the formation of kink bands and lateral matrix cracks. Lastly, the in-plane shear tests revealed failure initiating with longitudinal cracks in the V-notched region, progressing to pronounced in-plane shear cracks concentrated in the central portion of the sample.

The tensile tests provided insightful load–displacement curves, as shown in Fig. 4(a-b), for specimens oriented with fibres at 0° and 90°, respectively. As anticipated, the 0° orientation exhibited superior tensile performance, characterised by an initial linear response followed by abrupt load drops, likely due to localised failures occurring at varying load levels. Conversely, the 90° orientation demonstrated a nearly linear response with markedly lower strength and displacement at failure. Specifically, the tensile strength for the 0° samples X_{1t} was measured at 1374 ± 70 MPa, while the 90° samples X_{2t} showed a much lower strength of 43.4 ± 1.3 MPa.

To determine the elastic moduli, the stress–strain curves were analysed, as illustrated in Fig. 5(a-b). A strain range of 0.1% to 0.3%, where all curves exhibit linear behaviour, was used for modulus calculation. The analysis revealed a tensile modulus of 139.8 ± 10.9 GPa for the 0° samples and 7.1 ± 0.3 GPa for the 90° samples. These findings underscore the pronounced anisotropy in the mechanical properties of the material.

As anticipated, the compression tests yielded highly repeatable results. The corresponding compressive load–displacement curves for the two sample categories are presented in Fig. 6(a-b). The 90° samples exhibit pronounced non-linearity and variability in peak

Table 1
Optimum parameters used in each model.

Model	U_{max}/a	k/b	$t_0/c/n$	d
Sigmoidal (23 °C)	2.137	0.206	14.377	–
Sigmoidal (70 °C)	0.182	0.170	19.099	–
Polynomial (23 °C)	−0.083	0.046	0.004	−9.76E-05
Polynomial (70 °C)	0.005	−0.001	0.000	−7.13E-06
Exponential saturation (23 °C)	2.233	0.005	1.851	–
Exponential saturation (70 °C)	0.220	0.002	1.867	–

Table 2
Statistical metrics on the R^2 and root mean square error for each fitting model compared to experimental datapoints.

Model	R^2	RMSE
Sigmoidal (23 °C)	0.994	0.052
Sigmoidal (70 °C)	0.997	0.003
Polynomial (23 °C)	0.996	0.046
Polynomial (70 °C)	0.998	0.002
Exponential saturation (23 °C)	0.997	0.040
Exponential saturation (70 °C)	0.997	0.002

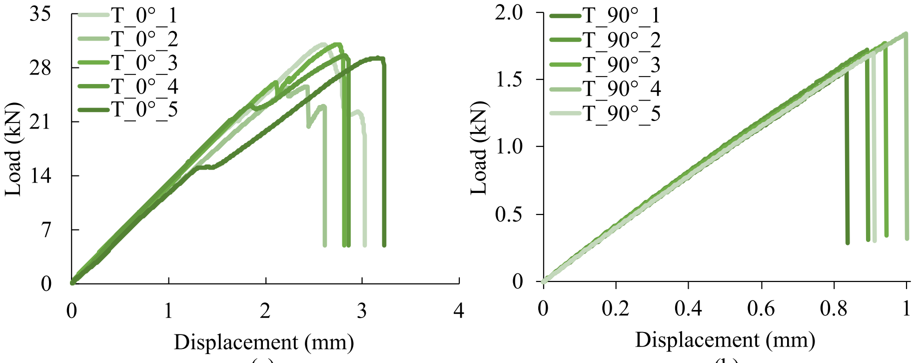

(a) (b)

Fig. 4. Load-displacement curves for tensile samples with fibres at (a) 0° and (b) 90°.

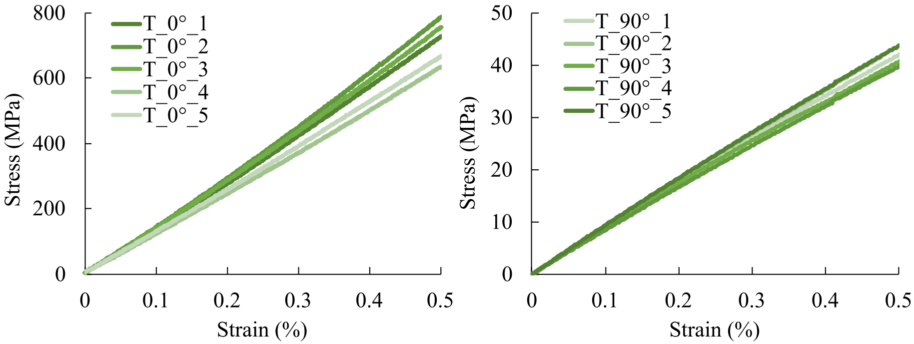

(a) (b)

Fig. 5. Stress–strain curves for tensile samples with fibres at (a) 0° and (b) 90°.

loads. In contrast, the 0° (longitudinal) samples demonstrate a highly linear response with more consistent peak load variations.

The in-plane shear load–displacement curves, illustrated in Fig. 7(a), display an initial linear region at low displacement levels, transitioning into a nonlinear regime characterised by two distinct load drops at varying load levels. These drops are attributed to the formation of localised cracks lateral to the load line near the notched regions, aligning with observations from previous studies [38,39]. It is important to note that shear strength is not assessed beyond these drops, as further loading results in the complete rupture of the samples. As depicted in Fig. 7(b), all samples failed at deformations below 5%, adhering to the standard limit for test termination.

5.3. *Fracture results*

5.3.1. *Mode-I fracture toughness*

The load–displacement curves for all samples – non-aged (NA) and aged at 23 °C and 70 °C – are presented in Fig. 8(a-c), showcasing the second phase of the test as detailed in Section 3.3. Every plot displays the results of five validated samples. The curves exhibit a quasi-linear region, culminating in a peak that signifies crack initiation and determines the load used to calculate the critical energy release rate. Beyond this peak, the curves transition to a non-linear regime corresponding to crack propagation. Notably, most samples demonstrate smooth crack propagation, devoid of abrupt load drops that would indicate unstable fracture behaviour.

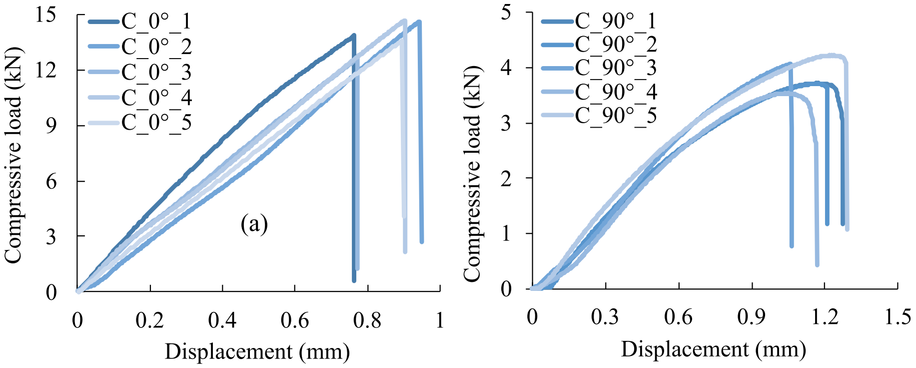

(a) (b)

Fig. 6. Load-displacement curves for compressive samples with fibres at (a) 0° and (b) 90°.

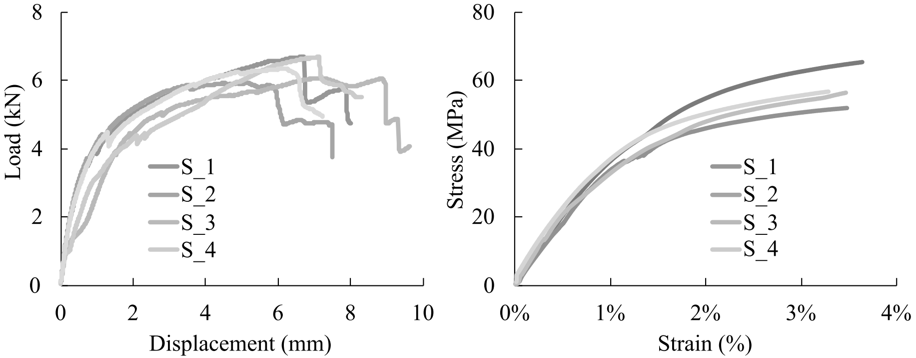

(a) (b)

Fig. 7. (a) Load-displacement and (b) stress–strain curves for the samples under shear loading.

However, the curves of samples aged at 70 °C reveal a markedly different morphology, characterised by a near-linear load decline, contrasting with the non-aged samples. This trend is mirrored in the G_I values, highlighting the influence of thermal ageing on fracture behaviour.

The R-curves presented in Fig. 9(a-c) illustrate the evolution of the critical energy release rate as a function of crack length for non-aged, aged at 23 °C, and aged at 70 °C, respectively. These curves provide valuable insights into the fracture toughness and crack propagation behaviour under different thermal ageing scenarios.

The non-aged samples exhibit a gradual increase in G_I with crack length, which is indicative of stable crack propagation. The curves display minimal scatter, demonstrating the consistency of fracture toughness in the absence of thermal ageing. This behaviour is characteristic of the baseline performance, with the quasi-linear increase in G_I, suggesting effective energy dissipation mechanisms and robust resistance to crack propagation. Overall, these *R*-curves have a slightly rising shape.

For the samples aged at 23 °C, the *R*-curves maintain a similar overall trend to the non-aged samples, with G_I increasing steadily with crack growth. However, the G_I values are slightly reduced across the crack length, highlighting a subtle decline in fracture toughness due to low-temperature ageing. This reduction could be attributed to minor matrix relaxation or interfacial degradation, which may occur even in moderate ageing conditions. Despite this, the ageing at 23 °C does not significantly alter the crack propagation characteristics, as the curves remain smooth and stable. In general, these *R*-curves have a flat shape.

The samples aged at 70 °C exhibit the most pronounced increase in G_I, with a rising *R*-curve shape that indicates significantly enhanced fracture toughness as crack propagation progresses. This behaviour suggests that ageing at higher temperatures has a toughening effect on the material due to a combined effect of matrix plasticisation and significant fibre bridging (discussed in detail in Section 5). The rising shape of the *R*-curves reflects the ability of the material to sustain higher energy release rates during crack propagation, pointing to increased resistance against fracture. Furthermore, the consistent upward trend across the samples indicates robust and stable crack propagation even under the influence of thermal ageing.

The critical energy release rate (G_{IC}) values (Table 3) demonstrate a clear trend influenced by ageing conditions. For non-aged samples, the average G_{IC} value is 377.7 ± 59.9 J/m^2, while samples aged at 23 °C exhibit a slight reduction to 333.8 ± 22.7 J/m^2. This decrease indicates minor degradation in fracture toughness under ambient ageing conditions, potentially due to moisture absorption or subtle matrix changes over time. Conversely, samples aged at 70 °C show a substantial increase in G_{IC} to 622.5 ± 54.3 J/m^2, suggesting that the elevated temperature may enhance crack resistance. This improvement could be attributed to the thermal post-

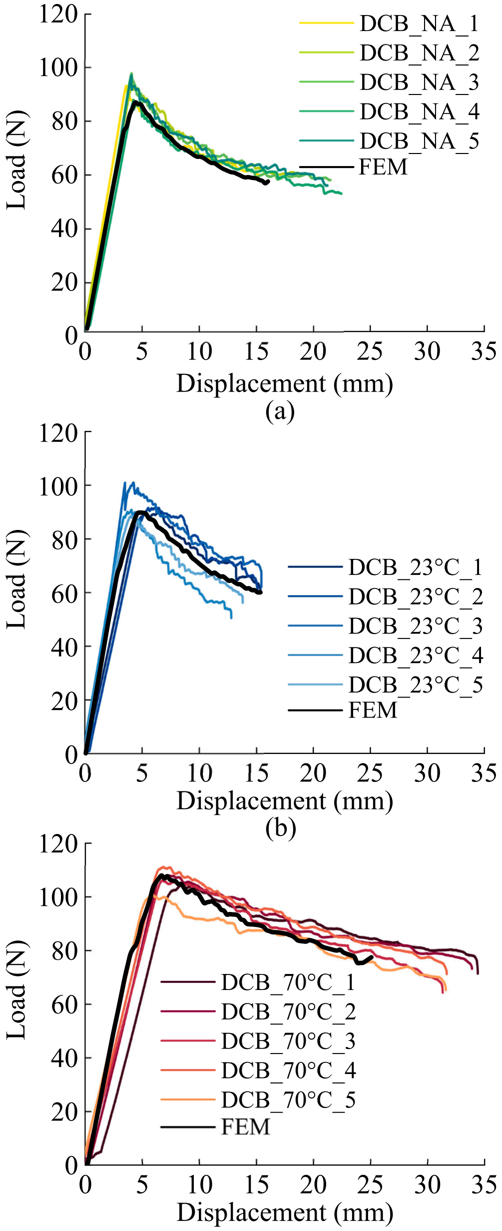

(a)

(b)

(c)

Fig. 8. Load–displacement curves for DCB samples under (a) non-aged, (b) aged at 23 °C, and (c) aged at 70 °C conditions. Each plot displays five replicates and the numerical prediction.

curing of the epoxy matrix, which can increase cross-link density and improve the interfacial adhesion between fibres and the matrix. However, the higher standard deviation for samples aged at 70 °C compared to non-aged and 23 °C-aged samples highlights the variability in the thermal ageing process, which may stem from heterogeneous heat diffusion or differences in initial manufacturing quality. While prolonged exposure to elevated temperatures can improve toughness through post-curing, it also introduces variability that could compromise reliability. Further interpretation of the phenomenon behind this gain in G_{IC} will be carried out by analysing images during DCB tests.

The load–displacement curves obtained from numerical modelling are presented along with the experimental ones in Fig. 8. The numerical results reflect effectively the tests in each of the configurations (unaged and aged at two temperatures). Thanks to the *R*-curve effect incorporation into the FE model, a gradual decrease in the force is observed, as it happens in the specimens tested experimentally. Exemplary results of the numerical analyses are presented in Fig. 10.

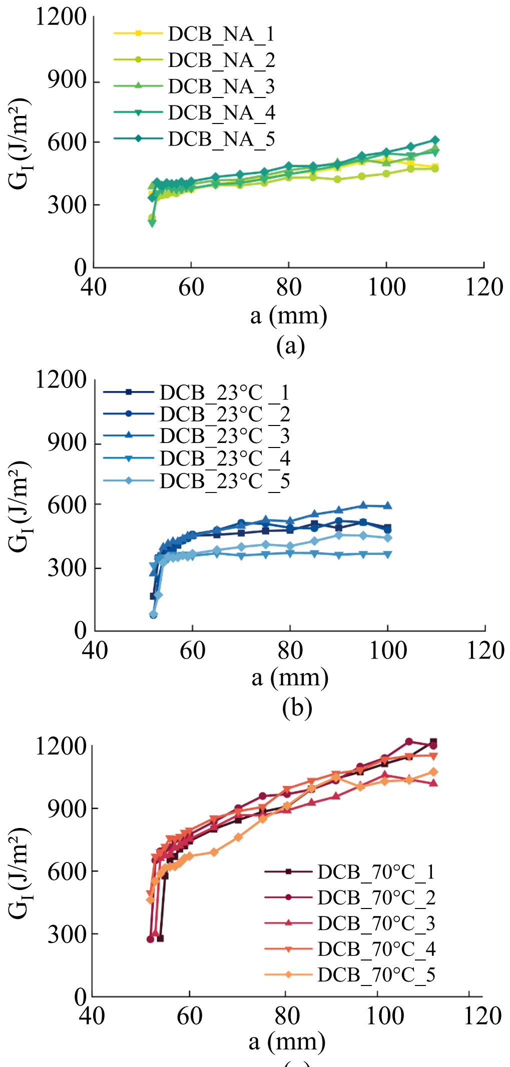

(a)

(b)

(c)

Fig. 9. *R*-curves for DCB samples (a) non-aged, (b) aged at 23 °C, and (c) 70 °C. Each plot displays five tested samples.

Table 3
Compilation of the elastic and strength constants for unaged samples.

Property	Value	
Longitudinal elastic modulus	E_1(GPa)	139.8 ± 10.9
Transverse elastic modulus	E_2(GPa)	7.1 ± 0.3
In-plane shear modulus	G_{12}(GPa)	4.3 ± 0.3
Major Poisson's ratio	ν_{12}	0.30 ± 0.02
Longitudinal tensile strength	X_{1t}(MPa)	1374.0 ± 70.0
Transverse tensile strength	X_{2t}(MPa)	43.4 ± 1.3
Longitudinal compressive strength	Y_{1c}(MPa)	762.6 ± 32.5
Transverse compressive strength	Y_{1c}(MPa)	133.4 ± 8.9
In-plane shear strength	S_{12}(MPa)	85.6 ± 3.9
Mode-I longitudinal fracture toughness	G_{IC}(J/m^2)	377.7 ± 59.9
Mode-II longitudinal fracture toughness	G_{IIC}(J/m^2)	1320.5 ± 61.0

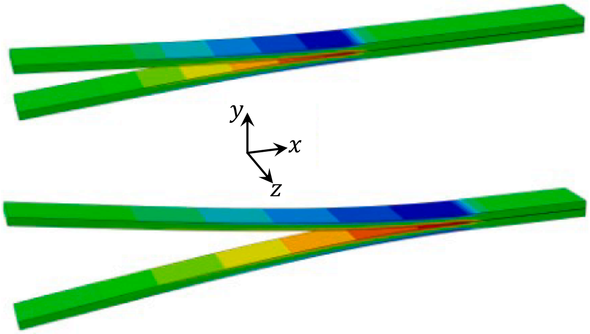

Fig. 10. FE simulation of the DCB test at two displacement stages: top corresponds to a displacement of 7.5 mm, and bottom to 21 mm. The plots show the stress distribution along the fibre direction (S11), highlighting the evolution of the delamination front and the stress redistribution during crack propagation under Mode I loading.

5.3.2. Mode-II fracture toughness

Fig. 11(a-c) presents the load–displacement curves obtained from tests for non-aged (NA) samples and samples aged at 23 °C and 70 °C, respectively. All tested specimens exhibit an initial linear region, corresponding to the elastic response, followed by a non-linear region leading to a peak load, which marks the onset of interlaminar crack propagation. Post-peak load, a gradual reduction in load indicates the progression of delamination under Mode-II loading.

The non-aged samples (Fig. 11(a)) demonstrate the highest peak loads, with minimal variability among replicates, indicating consistent interlaminar shear strength and toughness. The mechanical performance of these samples confirms that the material, in its pristine state, retains a high resistance to crack initiation and propagation.

Ageing under both 23 °C and 70 °C significantly impacts the interlaminar behaviour:

- 23 °C ageing: The peak loads for samples aged at 23 °C are noticeably reduced compared to the non-aged condition, suggesting environmental exposure causes degradation of interlaminar properties. This could result from minor moisture absorption or relaxation effects at the fibre/matrix interface, weakening the bonding and reducing shear resistance.
- 70 °C Ageing: These samples exhibit the lowest peak loads and a significant reduction in displacement at failure. This behaviour indicates severe degradation, likely due to the combined effects of thermal exposure and potential moisture absorption. High-temperature ageing may induce matrix softening, residual stresses, or fibre/matrix debonding, leading to diminished mechanical performance.

The observed reductions in peak load and displacement at failure with ageing highlight the material sensitivity to environmental conditions. Ageing at elevated temperatures (70 °C) leads to the most significant degradation, with reductions in both load-bearing capacity and interlaminar toughness. The consistent trends across replicates confirm the reliability of the observed behaviour.

The unconditioned samples exhibit a mean G_{IIC} of 1320.5 ± 61.0 J/m^2, establishing the baseline fracture toughness of the material in its pristine state. The low standard deviation suggests uniform interlaminar fracture behaviour among the specimens, indicative of a consistent manufacturing process and material quality. Samples conditioned at 23 °C display a mean G_{IIC} of 1322.6 ± 154.7 J/m^2, which is statistically comparable to the unconditioned samples within the observed variability. The higher standard deviation observed for the 23 °C samples suggests the presence of minor microstructural variations, potentially introduced by moisture absorption or relaxation effects at the fibre/matrix interface. However, the overall Mode-II fracture toughness remains statistically unaffected by ageing at this temperature.

A significant decrease in G_{IIC} is observed for samples aged at 70 °C, with a mean value of 1081.8 ± 132.9 J/m^2, corresponding to an approximate reduction of 18% compared to the unconditioned samples. The elevated standard deviation suggests that thermal exposure at 70 °C introduces microstructural heterogeneities, such as fibre/matrix interface degradation, thermal-induced residual stresses, or microcrack formation within the epoxy matrix. This behaviour is also likely due to the softening of the epoxy matrix and degradation at the fibre/matrix interface.

It is important to note that *R*-curves are not typically constructed for ENF tests. This configuration is designed to provide a single-point evaluation of the Mode II critical energy release rate, G_{IIC}, based on the onset of crack propagation. Unlike DCB tests, the ENF method does not support stable crack growth, which is a prerequisite for generating a valid resistance curve. Therefore, in this study, G_{IIC} was determined using a point-wise approach following the procedure provided in the ASTM D7905 standard.

The numerical simulations are presented alongside the experimental data in Fig. 11, demonstrating a strong correlation with the tested specimens. The FE results accurately capture the elastic response, closely mirroring the experimental curves while also effectively predicting the onset and progression of damage. Notably, the model successfully replicates the material degradation observed in the tests. Exemplary FEA results, highlighting the crack propagation and stress distribution, are showcased in Fig. 12. The delamination process was almost perfectly reflected in the simulation, and the front of the crack could be observed, as shown in Fig. 12 (a). Additionally, the stress distribution along the fibre direction (S11) is shown in Fig. 12 (b), reflecting the typical bending compressed

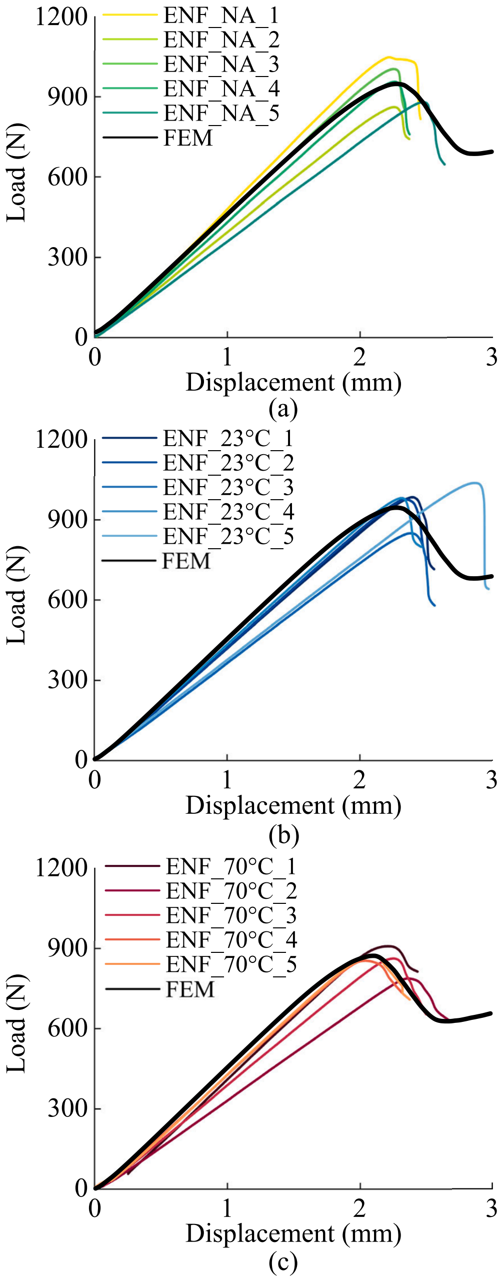

Fig. 11. Load–displacement curves for ENF samples under (a) non-aged, (b) aged at 23 °C, and (c) aged at 70 °C conditions. Each plot displays five samples and the numerical prediction.

(top surfaces, indicated in blue colour) and stretched (bottom surfaces, indicated in red colour) areas of the specimen.

6. Discussion

Table 3 compiles the elastic and strength constants calculated from the quasi-static tensile, compressive, and in-plane shear tests presented in Section 4.2. These results are extremely useful as they provide the full set of input constants required for FE simulations of composite materials. The elastic and strength allowables presented in Table 3 are used as input in the FE models of this work, in which the composite laminate was treated as a transversely isotropic material, which is a suitable assumption for unidirectional fibre-reinforced composites exhibiting in-plane isotropy. This assumption reduces the number of independent elastic constants required to define the constitutive behaviour, as $E_2 = E_3$, $G_{12} = G_{13}$ and $\nu_{12} = \nu_{13}$. This approach ensures a realistic yet computationally efficient representation of the laminate behaviour while avoiding the need for a fully orthotropic material definition.

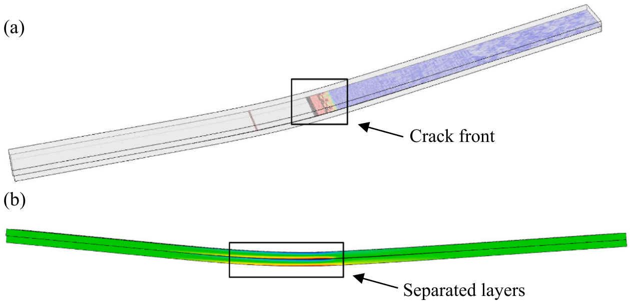

Fig. 12. The ENF numerical model: Representative results illustrating the crack front progression during (a) delamination and (b)stress distribution across the separated layers.

Now, analysing the failure mechanisms of the samples used to characterise interlaminar fracture toughness under Mode I and II loading is essential, as clear and distinct differences emerge between samples aged at 23 °C and 70 °C.

The variation in Mode I crack opening can be observed in Fig. 13, which compares the behaviour of composite DCB samples subjected to hygrothermal ageing at 25 °C (a) and 70 °C (b). The most notable distinction lies in the presence of pronounced fibre bridging, which, as depicted in the figure, is significantly more intense in the sample exposed to moisture at elevated temperatures.

Fibre bridging in unidirectional (UD) composites is often rooted in the nesting phenomenon [36]. This occurs during the curing process when pressure is applied to the composite structure, causing fibres to interlock between adjacent layers. Additionally, the fibre/matrix interface plays a pivotal role in the development of fibre bridging, particularly in longitudinal (0°) UD plies. Potential interface debonding may facilitate the partial detachment of fibre bundles, which then become distributed between the two halves of the composite laminate. This behaviour aligns with findings from Sakai et al. [37] and Crews et al. [38].

In a similar context, Khan et al. [39] observed the fibre-bridging effect during the introduction of a fatigue crack, concluding that, despite the fibres connecting the two halves of the component, the crack plane remained unchanged. Generally, fibre bridging tends to enhance the energy release rate in both Mode I and Mode II crack openings, particularly during crack propagation, as noted by Shokrieh et al. [40]. Under static loading, the increased yielding in the region beyond the crack tip, which extends across multiple layers, may cause the crack tip to migrate to an adjacent layer, as reported in [41]. This reorientation of the crack front results in greater energy dissipation. Zimmermann and Wang [42] highlighted that multiple failure modes can coexist in Mode I crack opening, potentially affecting the test results and the purity of the data obtained.

In the present study, the unidirectional (UD) composite samples exhibited crack plane deviation, as illustrated in Fig. 14. Here, the crack briefly deviated from its initial plane, propagated through an adjacent layer, and subsequently realigned with the original plane after a short distance.

In addition to the two phenomena discussed, the combined effects of temperature and moisture exposure emerge as critical factors influencing the fracture toughness of composite laminates. Environmental conditions are widely recognised as pivotal in affecting fracture toughness, whether in flat laminates [41,42] or curved composite samples [27]. Pollet et al. [29] specifically noted that ageing in high-temperature environments increases the susceptibility of samples to delamination by degrading the fibre/matrix interface, which in turn reduces energy release values.

The interplay of these mechanisms shapes the morphology of the *R*-curves presented in Section 4.3.1. Notably, the energy release rates associated with crack initiation are consistently lower than those of crack propagation. This trend is partly attributed to fibre bridging, a characteristic feature of 0° UD composite structures, which contributes to elevated energy release rate values during crack propagation across all scenarios. However, water exposure intensifies fibre/matrix debonding, making fibre bridging more pronounced in the 70 °C specimens.

Additionally, variations in matrix quality must be considered, as crack plane deviations were observed at specific distances from the

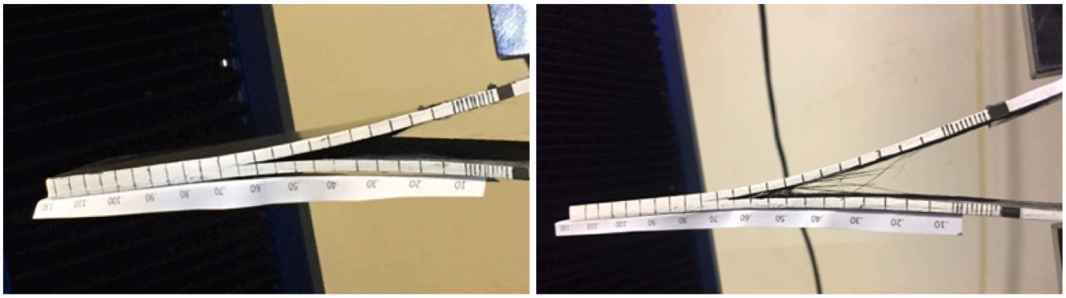
(a) (b)

Fig. 13. Moments capturing the initiation of a Mode-I crack opening in DCB samples conditioned under humidity at (a) 23 °C and (b) 70 °C.

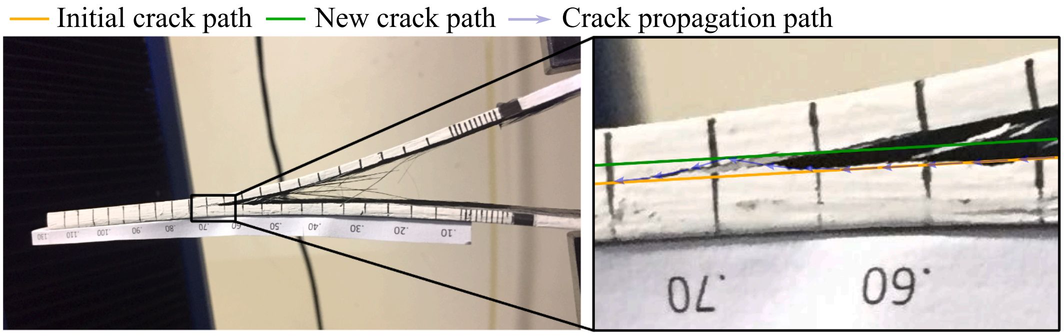

Fig. 14. Crack path deviation and plane migration in a UD composite sample subjected to 70 °C moisture under mode I crack opening.

initial crack length. Moisture absorption weakens the ply-ply interface, leading to reduced G_I and G_{II} values. Consequently, samples exposed to lower humidity levels at 23 °C demonstrated higher fracture toughness compared to those subjected to elevated temperatures. This highlights the critical role of environmental factors in determining the mechanical performance of composite laminates.

Scanning electron microscopy (SEM) images were taken to further understand the consequences of ageing. To analyse them on a fair and equal basis, the images were analysed through the Python Imaging Library (PIL package), which has powerful image processing capabilities. In this way, there is no room for interpretation when it comes to differences in failure mechanisms in the images. Representative images of the non-aged and aged at 70°C of the DCB samples are presented in Fig. 15.

By interpreting these images, the following observations can be made:

1. Matrix cracking:
- Microcracks in the matrix: The fracture surface appears to show signs of matrix cracking, especially along the resin-rich areas, which is typical for non-aged composite materials. These cracks propagate along the matrix without significant fibre involvement.
- Interlaminar cracking: This can be seen as cracks running parallel to the fibre direction, indicating that the bonding between the matrix and fibres or the interface between layers is weak under stress.
2. Fibre pull-out:
- Unbroken fibre ends: In some regions, fibres are pulled out from the matrix, leaving behind traces of resin on their surfaces. This indicates that the fibres are not fully bonded with the matrix, which allows them to be extracted during crack propagation, characteristic of a ductile matrix failure.
- Pull-out lengths: The fibres that are pulled out show varying lengths, suggesting that the crack propagated through the matrix without significant fibre bridging. This is typical of the failure mode in non-aged composites where fibres do not play an active role in delaying crack growth.
3. Fibre breakage:
- Fibre fracture: Some fibres appear to have broken during the fracture process. This indicates that, in addition to matrix failure, there is some degree of failure in the fibres themselves. This can happen under high loads or localised stress concentrations.
4. Debonding at fibre–matrix interface:
- Interface failure: The fibre–matrix interface may be seen to separate in some regions, indicating debonding. This is a typical failure mode in composites, especially when the interface strength is lower than that of the fibre or matrix.

The annotated SEM image of the aged DCB sample shows the following fracture features:

- Matrix cracking: Areas where cracks in the matrix are prominent, indicating damage propagation primarily through the matrix.
- Fibre pull-out: Regions where fibres have been pulled out of the matrix, suggesting weakened fibre–matrix bonding due to ageing.
- Fibre bridging: Indications of fibres spanning across the fracture surface, resisting crack propagation, a feature unique to the aged sample.
- Fibre-Matrix debonding: Locations showing separation between fibres and the matrix, a characteristic of interface degradation due to ageing.

As illustrated in the figure, the two representative samples exhibit common failure mechanisms, including fibre/matrix debonding, matrix cracking, and fibre pull-out. However, in the aged sample, the dominant failures are predominantly associated with fibre pull-out, likely a consequence of more pronounced fibre/matrix debonding compared to the non-aged counterpart, alongside fibre bridging. Notably, this latter feature aligns closely with the macroscopic observations recorded during testing.

The effect of hygrothermal ageing on mode II fracture behaviour of carbon/epoxy composites is evidenced in the SEM micrographs in Fig. 16. The non-aged sample demonstrates classical features of shear-driven failure, with fibre pull-out and well-defined matrix shear hackles, which indicate effective interfacial bonding and a relatively brittle fracture. These features are typically associated with higher interlaminar fracture toughness. Conversely, the aged sample subjected to 70 °C exhibits significant morphological changes, including widespread matrix smearing, debris formation, and some fibre–matrix debonding. These are evidence of matrix

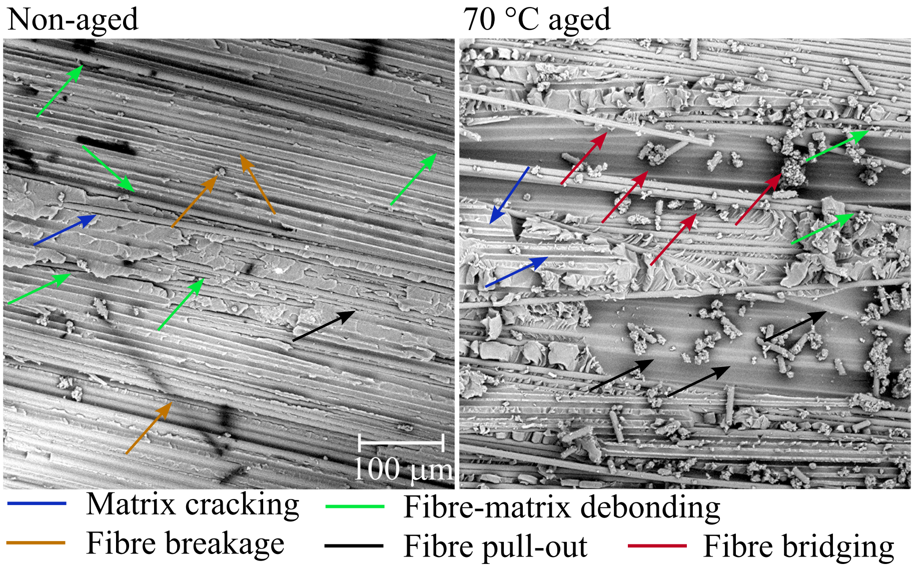

Fig. 15. SEM images of fractured DCB samples taken 10 mm after the crack tip for (left) non-aged and (right) aged at 70 °C.

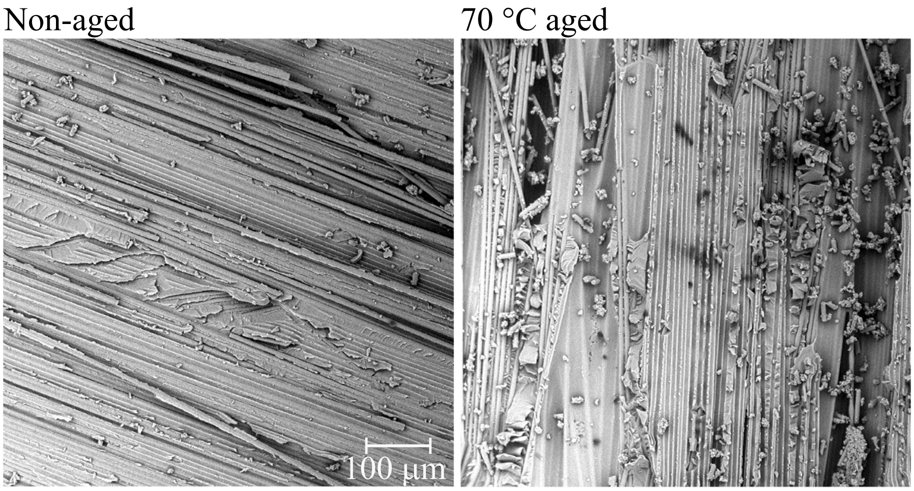

Fig. 16. SEM micrographs of fracture surfaces from mode II interlaminar fracture toughness (ENF) tests on carbon/epoxy composites: (left) non-aged and (right) aged at 70 °C.

plasticisation and hydrolytic degradation processes induced by prolonged exposure to high temperature and moisture. The rougher fracture surface and apparent reduction in interfacial adhesion in the aged samples are consistent with the observed reduction in mode II fracture toughness, as the crack propagation occurs more easily through the weakened matrix–fibre interface.

Overall, the non-aged composite was able to resist crack propagation more effectively. On the other hand, the 70 °C aged composite experienced degradation of the matrix and of the fibre–matrix interface, resulting in reduced mode II fracture toughness (G_{IIC}) due to a lower resistance to shear crack propagation.

7. Conclusions

This study investigated the effects of hygrothermal ageing on the fracture behaviour of filament-wound carbon/epoxy composites, focusing on Mode I and Mode II mechanisms through DCB and ENF tests. Mechanical characterisation under tension, compression, and shear provided a comprehensive understanding of the material response, useful for further computational modelling of composite structures made of this material system.

Results revealed a contrasting influence of ageing. While room-temperature exposure had minimal impact on Mode I behaviour, ageing at 70 °C significantly enhanced Mode I fracture toughness due to fibre bridging, as confirmed by real-time observations and post-mortem SEM analysis. Conversely, Mode II toughness deteriorated under the same conditions due to severe matrix cracking and fibre/matrix debonding, highlighting a trade-off between improved fibre bridging and matrix degradation.

Finite element simulations showed excellent agreement with experimental data, particularly when incorporating the *R*-curve effect in DCB analysis, accurately capturing crack initiation and propagation. These findings offer valuable insights into the durability of filament-wound composites under hygrothermal conditions and pave the way for future research on multi-environmental ageing and micromechanical degradation mechanisms.

CRediT authorship contribution statement

Leonardo G. Schreer: Investigation, Formal analysis. **Antonios G. Stamopoulos:** Writing – original draft, Visualization, Investigation. **Paweł Stabla:** Visualization, Software, Investigation. **Michał Smolnicki:** Validation, Software, Investigation. **Sandro C. Amico:** Writing – review & editing, Supervision, Resources, Project administration, Funding acquisition. **José Humberto S. Almeida:** Conceptualization, Data curation, Investigation, Methodology, Software, Validation, Visualization, Writing – original draft.

Declaration of competing interest

The authors declare that they have no known competing financial interests or personal relationships that could have appeared to influence the work reported in this paper.

Acknowledgements

SC Amico would like to thank CNPq, CAPES and FAPERGS for the financial support of this work.

Data availability

Data will be made available on request.

References

[1] Moazzami M, Ayatollahi MR, Akhavan-Safar A, Freitas ST, Poulis JA, da Silva LFM. Effect of cyclic aging on mode I fracture energy of dissimilar metal/composite DCB adhesive joints. Engng Fract Mech 2022;271:108675. https://doi.org/10.1016/j.engfracmech.2022.108675.

[2] Jia R, Zhao L, Curti R, Gong X. Determination of pure mode-I fracture toughness of multidirectional composite DCB specimens. Engng Fract Mech 2021;252:107776. https://doi.org/10.1016/j.engfracmech.2021.107776.

[3] Azevedo CB, Almeida Jr JHS, Flores HF, Eggers F, Amico SC. Influence of mosaic pattern on hygrothermally-aged filament wound composite cylinders under axial compression. J Compos Mater 2020;54(19):2651–9. https://doi.org/10.1177/0021998319899144.

[4] Natale E, Gaspari A, Chiominto L, D'Emilia G, Stamopoulos AG. Morphological analysis of as-manufactured filament wound composite cylinders using contact and non-contact inspection methods. Engng Fail Anal 2024;158:108011. https://doi.org/10.1016/j.engfailanal.2024.108011.

[5] Eggers F, Almeida Jr JHS, Lisbôa TV, Amico SC. Creep and residual properties of filament-wound composite rings under radial compression in harsh environments. Polymers 2021;13(1):33. https://doi.org/10.3390/polym13010033.

[6] Almeida Jr JHS, Lisboa TV, Spickenheuer A, St-Pierre L. A sequential finite element model updating routine to identify creep parameters for filament wound composite cylinders in aggressive environments. Comput Struct 2023;276:106939. https://doi.org/10.1016/j.compstruc.2022.106939.

[7] Srivastava C, Agostino P, Stamopoulos AG, Alcock B, Strandlie A, Grammatikos S. Three-dimensional analysis of porosity in as-manufactured glass fibre/vinyl ester filament winded composites using x-ray micro-computed tomography. Appl Compos Mater 2024;31(1):171–200. https://doi.org/10.1007/s10443-023-10167-z.

[8] De Menezes EAW, Lisboa TV, Almeida Jr JHS, Spickenheuer A, Amico SC, Marczak RJ. On the winding pattern influence for filament wound cylinders under axial compression, torsion, and internal pressure loads. Thin-Walled Struct 2023;191:111041. https://doi.org/10.1016/j.tws.2023.111041.

[9] Dai Y, Zheng C, Lin J, Liu Y, Wang D, Lu J. Winding pattern design of composite cylinders considering the effect of fibre stacking. Compos B 2024;275:111306. https://doi.org/10.1016/j.compositesb.2024.111306.

[10] Braiek S, Ben KA, Zitoune R, Zidi M. Experimental and numerical investigation of adhesively bonded 55° filament wound tubular specimens under internal pressure. Engng Fract Mech 2018;199:461–75. https://doi.org/10.1016/j.engfracmech.2018.06.009.

[11] Antunes MB, Almeida Jr JHS, Amico SC. Curing and seawater aging effects on mechanical and physical properties of glass/epoxy filament wound cylinders. Compos Commun 2020;22:100517. https://doi.org/10.1016/j.coco.2020.100517.

[12] He X, Shi Y, Kang C, Yu T. Analysis and control of the compaction force in the composite prepreg tape winding process for rocket motor nozzles. Chin J Aeronaut 2017;30(2):836–45. https://doi.org/10.1016/j.cja.2016.07.004.

[13] Dao B, Hodgkin J, Krstina J, Mardel J, Tian W. Accelerated ageing versus realistic ageing in aerospace composite materials. III. The chemistry of thermal ageing in bismaleimide based composites. J Appl Polymer Sci 2007;154(4), 2062-2072. DOI: 10.1002/app.26320.

[14] Yesu A, Srivastava M, Agnihotri PK, Basu S. Minimizing environmental degradation in fracture toughness of carbon fiber/epoxy composites using carbon nanotubes. Engng Fract Mech 2023;294:109734. https://doi.org/10.1016/j.engfracmech.2023.109734.

[15] Garg A, Chalak HD. A review on analysis of laminated composite and sandwich structures under hygrothermal conditions. Thin-Walled Struct 2019;142:205–26. https://doi.org/10.1016/j.tws.2019.05.005.

[16] Tsokanas P, Loutas T. Hygrothermal effect on the strain energy release rates and mode mixity of asymmetric delaminations in generally layered beams. Engng Fract Mech 2019;214:390–409. https://doi.org/10.1016/j.engfracmech.2019.03.006.

[17] Christoff BG, Almeida Jr JHS, Ribeiro ML, Maciel MM, Guedes RM, Tita V. Multiscale modelling of composite laminates with voids through the direct FE^2 method. Theor Appl Fract Mech 2024;131:104424. https://doi.org/10.1016/j.tafmec.2024.104424.

[18] Mujika F, Tsokanas P, Arrese A, Valvo PS, da Silva LFM. Mode decoupling in interlaminar fracture toughness tests on bimaterial specimens. Engng Fract Mech 2023;290. https://doi.org/10.1016/j.engfracmech.2023.109454.

[19] Davidson BD, Kumar M, Soffa MA. Influence of mode ratio and hygrothermal condition on the delamination toughness of a thermoplastic particulate interlayered carbon/epoxy composite. Compos A 2009;40:67–79. https://doi.org/10.1016/j.compositesa.2008.10.006.

[20] Sezler R, Friedrich K. Mechanical properties and failure behaviour of carbon fibre-reinforced polymer composites under the influence of moisture. Compos A 1997;28(6):595–604. https://doi.org/10.1016/S1359-835X(96)00154-6.

[21] Garg A, Ishai O. Hygrothermal influence on delamination behavior of graphite/epoxy laminates. Engng Fract Mech 1985;22(3):413–27. https://doi.org/10.1016/0013-7944(85)90142-0.

[22] Chr F, Arendts FJ. Electrical crack length measurement and the temperature dependence of the Mode I fracture toughness of carbon fibre reinforced plastics. Compos Sci Technol 1993;46(4):319–23. https://doi.org/10.1016/0266-3538(93)90177-I.

[23] Khan LA, Mahmood AH, Syed AS, Khan Z, Day RJ. Effect of hygrothermal conditioning on the fracture toughness of carbon/epoxy composites cured in autoclave/Quickstep. J Reinf Plast Compos 2013;32(16):1165–76. https://doi.org/10.1177/0731684413486367.

[24] Foral RF. Delamination failures in curved composite laminates. Key Engng Mater 1989;37:137–48. https://doi.org/10.4028/www.scientific.net/ KEM.37.137.

[25] Ozdil F, Carlsson LA. Characterization of mode I delamination growth in glass/epoxy composite cylinders. J Compos Mater 2020;34(5):398–419. https://doi.org/10.1177/002199830003400503.

[26] Perillo G, Echtermeyer AT. Mode-I fracture toughness testing of composite pipes. Appl Compos Mater 2013;20:1135–46. https://doi.org/10.1007/s10443-013-9318-7.

[27] Abd Rased MF, Yoon SH. Experimental study on effects of asymmetrical stacking sequence on carbon fibre/epoxy filament wound specimens in DCB, ENF, and MMB tests. Compos Struct 2020;264:113749. https://doi.org/10.1016/j.compstruct.2021.113749.

[28] Taylor JM, Frenz S, Canturri C, Giannis S, Greenhalgh ES. Mode-I and Mode-II fracture behaviour of carbon/glass hybrid filament-wound resin transfer moulded composites. Proceedings of the 16th European Conference on Composite Materials ECCM16, 22-26 June 2014, Seville, Spain.

[29] Pollet A, Almeida Jr JHS, Stamopoulos AG, Amico SC. Mode-I fracture toughness of hygrothermally aged curved filament-wound carbon and glass fibre composites. Engng Fail Anal 2024;160:108172. https://doi.org/10.1016/j.engfailanal.2024.108172.

[30] Arellano MT, Crouzeix L, Douchin B, Collombet F, Hernández MH, González VJ. Strain field measurement of filament-wound composites at $\pm 55^{o}$ using digital image correlation: an approach for unit cells employing flat specimens. Compos Struct 2010;92:2457–64. https://doi.org/10.1016/j.compstruct.2010.02.014.

[31] Shalom S, Harel H, Marom G. Fatigue behaviour of flat filament-wound polyethylene composites. Compos Sci Technol 1997;57:1423–7. https://doi.org/10.1016/S0266-3538(97)00084-5.

[32] Ribeiro ML, Vandepitte D, Tita V. Damage model and progressive failure analysis for filament wound composite laminates. Appl Compos Mater 2013;20:975–92. https://doi.org/10.1007/s10443-013-9315-x.

[33] Almeida Jr JHS, Souza SDB, Botelho EC, et al. Carbon fiber-reinforced epoxy filament-wound composite laminates exposed to hygrothermal conditioning. J Mater Sci 2016;51:4697–708. https://doi.org/10.1007/s10853-016-9787-9.

[34] Stamopoulos AG, Psaropoulos AP, Tserpes K. Experimental and numerical investigation of the effects of porosity on the in-plane shear properties of CFRPs using the V-notched rail shear test method. Int J Mater Form 2021;14:67–82. https://doi.org/10.1007/s12289-020-01544-1.

[35] Smolnicki M, Duda S, Zielonka P, Stable P, Lesiuk G, Lopes CCC. Combined experimental–numerical mode I fracture characterization of the pultruded composite bars. Arch Civ Mech Engng 2023;23:1–11. https://doi.org/10.1016/B978-0-08-102679-3.00008-3.

[36] Johnson WS, Mangalgiri PD. Investigation of fibre bridging in double cantilever beam specimens. J Compos Tech Res 1987;9(1):10–3. https://doi.org/10.1520/ctr10421j.

[37] Sakai M, Miyajima T, Inagaki M. Fracture toughness and fibre bridging of carbon fibre reinforced carbon composites. Compos Sci Technol 1991;40(3):231–50. https://doi.org/10.1016/0266-3538(91)90083-2.

[38] Crews JH, Shivakumar K, Raju I. A fibre-resin micromechanics analysis of the delamination front in a DCB specimen. NASA Tech Memo 1988;100540(44).

[39] Khan R, Alderliesten R, Badshah S, Khattak MA, Khan MS, Benedictus R. Experimental investigation of the microscopic damage development at mode I fatigue delamination tips in carbon/epoxy laminates. Jurnal Teknologi 2016;78(11). https://doi.org/10.11113/.v78.8072.

[40] Shokrieh M, Heidari-Rarani M, Ayatollahi M. Delamination R-curve as a material property of unidirectional glass/epoxy composites. Mater Des 2018;34:211–8. https://doi.org/10.1016/j.matdes.2011.08.006.

[41] Khan R. Fibre bridging in composite laminates: a literature review. Compos Struct 2019;229. https://doi.org/10.1016/j.compstruct.2019.111418.

[42] Zimmermann N, Wang PH. A review of failure modes and fracture analysis of aircraft composite materials. Engng Fail Anal 2020;115:104692. https://doi.org/10.1016/j.engfailanal.2020.104692.